Received: 29 March 2024 | Accepted: 18 June 2024

DOI: 10.1002/hem3.142

ARTICLE

HemaSphere EHA EUROPEAN HEMATOLOGY ASSOCIATION

PD-L1^{+} macrophage and tumor cell abundance and proximity to T cells in the pretreatment large B-cell lymphoma microenvironment impact CD19 CAR-T cell immunotherapy efficacy

Alexandre V. Hirayama[1,2,3,^] | Jocelyn H. Wright[1,^] | Kimberly S. Smythe[4] | Salvatore Fiorenza[1,5] | Akira N. Shaw[5] | Jordan Gauthier[1,2,3] | David G. Maloney[2,3,4] | Kikkeri N. Naresh[3,4,6,^] | Cecilia C. S. Yeung[3,4,6,^] | Cameron J. Turtle[2,3,4,5]

Graphical Abstract

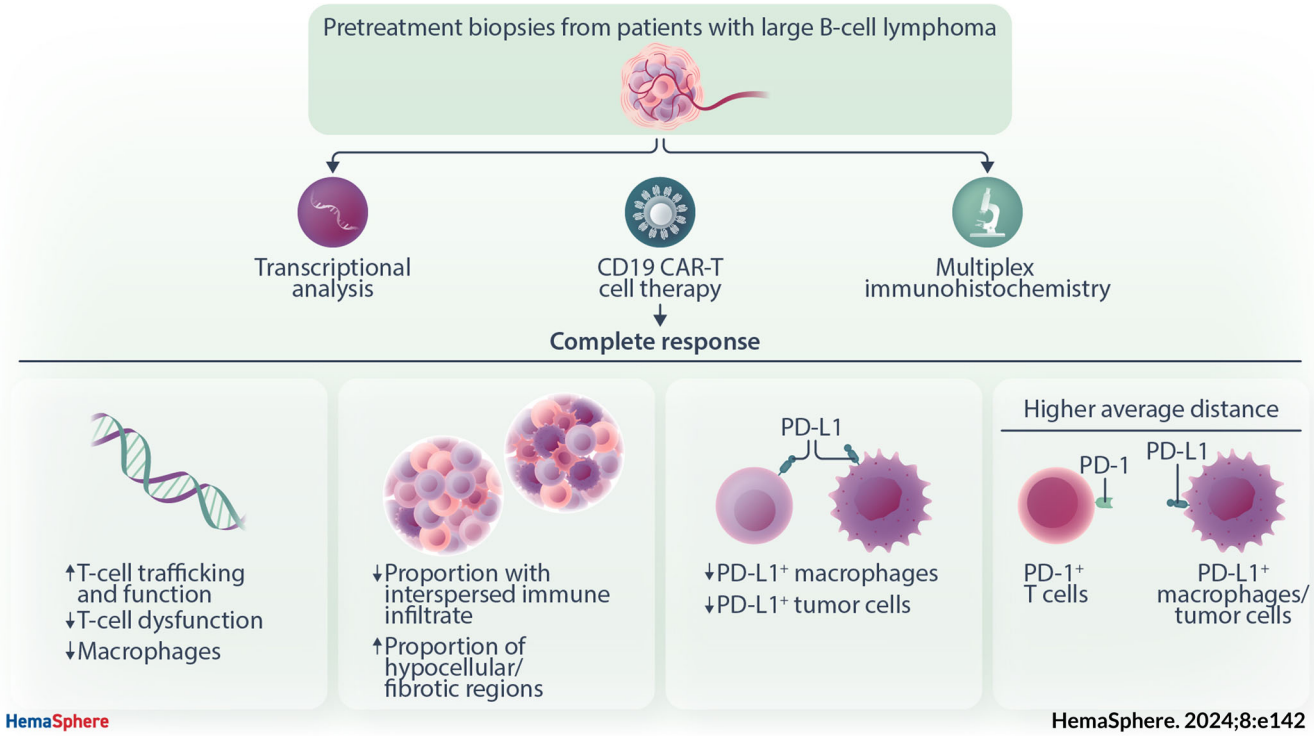

Received: 29 March 2024 | Accepted: 18 June 2024

DOI: 10.1002/hem3.142

ARTICLE

HemaSphere EHA EUROPEAN HEMATOLOGY ASSOCIATION

PD-L1$^+$ macrophage and tumor cell abundance and proximity to T cells in the pretreatment large B-cell lymphoma microenvironment impact CD19 CAR-T cell immunotherapy efficacy

Alexandre V. Hirayama[1,2,3,^] | **Jocelyn H. Wright**[1,^] | **Kimberly S. Smythe**[4] | **Salvatore Fiorenza**[1,5] | **Akira N. Shaw**[5] | **Jordan Gauthier**[1,2,3] | **David G. Maloney**[2,3,4] | **Kikkeri N. Naresh**[3,4,6,^] | **Cecilia C. S. Yeung**[3,4,6,^] | **Cameron J. Turtle**[2,3,4,5]

Correspondence: Alexandre V. Hirayama (ahirayama@fredhutch.org)

Abstract

CD19-targeted chimeric antigen receptor T-cell (CAR-T) immunotherapy has transformed the management of relapsed/refractory large B-cell lymphoma (LBCL), yet durable remissions are observed in less than half of treated patients. The tumor microenvironment (TME) is a key and understudied factor impacting CD19 CAR-T therapy outcomes. Using NanoString nCounter transcriptome profiling ($n = 24$) and multiplex immunohistochemistry (mIHC, $n = 15$), we studied the TME in pretreatment biopsies from patients with LBCL undergoing CD19 CAR-T therapy. Patients who achieved complete response (CR) after CAR-T therapy demonstrated higher expression of genes associated with T-cell trafficking and function, whereas those who did not achieve CR had higher expression of genes associated with macrophages and T-cell dysfunction. Distinct patterns of immune infiltration and fibrosis in the TME were associated with CAR-T therapy outcomes, and these findings were corroborated using artificial intelligence-assisted image analyses. Patients who achieved CR had a lower proportion of the biopsy occupied by an interspersed immune infiltrate and a higher proportion of hypocellular/fibrotic regions. Furthermore, mIHC revealed lower density of CD4$^+$ T cells and higher densities of both macrophages and tumor cells expressing PD-L1 in non-CR patients. Spatial analysis revealed that PD-1$^+$ T cells were in close proximity to PD-L1$^+$ macrophages or PD-L1$^+$ tumor cells in patients who did not compared to those who did achieve CR after CAR-T therapy. These findings suggest that morphologic patterns in the TME and engagement of the PD-1/PD-L1 axis in pretreatment biopsies may impact CD19 CAR-T immunotherapy response in patients with LBCL.

INTRODUCTION

CD19-targeted chimeric antigen receptor (CAR)-T cell immunotherapy has transformed the treatment of patients with relapsed and/or refractory (R/R) large B-cell lymphoma (LBCL). However, durable remissions are observed in less than half of treated patients.[1–7] Loss of tumor antigen expression,[8] dysfunction of infused CAR-T cells,[9,10] and suppressive factors in the tumor microenvironment (TME) are potential mechanisms of failure.[11–13]

[1]Clinical Research Division, Fred Hutchinson Cancer Center, Seattle, Washington, USA
[2]Department of Medicine, University of Washington, Seattle, Washington, USA
[3]Integrated Immunotherapy Research Center, Fred Hutchinson Cancer Center, Seattle, Washington, USA
[4]Translational Science and Therapeutics Division, Fred Hutchinson Cancer Center, Seattle, Washington, USA
[5]Faculty of Medicine and Health, The University of Sydney, Camperdown, New South Wales, Australia
[6]Department of Laboratory Medicine and Pathology, University of Washington, Seattle, Washington, USA
^Alexandre V. Hirayama, Jocelyn H. Wright, Kikkeri N. Naresh, and Cecilia C. S. Yeung contributed equally to this work.

This is an open access article under the terms of the Creative Commons Attribution-NonCommercial-NoDerivs License, which permits use and distribution in any medium, provided the original work is properly cited, the use is non-commercial and no modifications or adaptations are made.
© 2024 The Author(s). *HemaSphere* published by John Wiley & Sons Ltd on behalf of European Hematology Association.

In patients with newly diagnosed LBCL, gene expression profiling (GEP) of pretreatment biopsies has revealed a functional relationship between stromal elements, the composition of the TME, the immune milieu, and outcomes after chemoimmunotherapy.[14–17] Studies utilizing flow cytometry and immunohistochemistry (IHC) in pretreatment LBCL biopsies also identified predictors of outcomes. For instance, in patients treated with R-CHOP, $CD4^+$ T-cell infiltration was associated with longer survival.[18] The role of tumor-associated macrophages (TAMs) remains uncertain due to conflicting findings across studies; however, a higher density of $CD68^+CD163^+$ M2 TAMs was associated with poor overall survival in a meta-analysis.[19] Moreover, programmed cell death-ligand 1 (PD-L1) and its T-cell inhibitory receptor, programmed cell death-1 (PD-1), are expressed in the TME in a subset of LBCL biopsies, with PD-$L1^+$ LBCL,[20] and higher T-cell PD-1^+ expression, and cell density[21] associated with worse survival.

Characteristics of the R/R LBCL TME that might impact outcomes after CD19 CAR-T cell immunotherapy have just begun to be explored. In pretreatment biopsies, lower expression of interferon signaling genes,[13] and higher gene expression of cytokines and chemokines that favor T-cell infiltration,[22] and T-cell and stroma-associated genes,[23] were associated with favorable responses. Furthermore, pretreatment biopsies of responding patients also had a higher density of $CD8^+$ T cells with an activated phenotype (PD-$1^+LAG^{+/-}TIM3^-$)[22] and a lower density of $CD163^+$ macrophages expressing PD-L1 or IDO1.[23]

Here, we report findings from the analyses of GEP and multiplex immunohistochemistry (mIHC) with in-depth characterization of tumor architecture and infiltrate patterns in the TME of biopsies collected before lymphodepletion (LD) in patients with LBCL undergoing CD19 CAR-T cell immunotherapy. In pretreatment tumor biopsies, we not only identified gene signatures and immune cell densities associated with response but also distinct morphologic patterns of immune cell infiltration and fibrosis. Additionally, we found that the spatial proximity of PD-$L1^+$ macrophages and tumor cells to PD-1^+ T cells in the TME was associated with inferior outcomes after CD19 CAR-T cell immunotherapy.

MATERIALS/SUBJECTS AND METHODS

Analysis of clinical trial samples

CAR-T cell enumeration was assessed by flow cytometry, as previously described, in 40 patients with R/R LBCL treated with cyclophosphamide and fludarabine LD followed by infusion of 2×10^6 CAR T cells/kg on a previously reported phase 1/2 clinical trial of CD19 CAR-T cell immunotherapy (NCT01865617).[1,24,25]

Biopsy samples and clinical outcomes

Samples were collected before LD from patients with R/R LBCL treated with defined composition autologous CD19 CAR T cells containing a 4-1BB costimulatory domain in three early-phase investigator-initiated clinical trials (NCT01865617, NCT02706405, NCT03103971; www.clinicaltrials.gov). Response was assessed by positron emission tomography (PET) and concurrent diagnostic-quality computed tomography (PET/CT) and was evaluated centrally according to the Lugano criteria.[26] The studies were performed in accordance with the Declaration of Helsinki, with the approval of the Fred Hutchinson Cancer Center Institutional Review Board. All participants provided written informed consent.

Gene expression profiling (GEP)

RNA was extracted from formalin-fixed paraffin-embedded (FFPE) tissue slides/curls with the Qiagen RNeasy FFPE Kit (Qiagen). Digital GEP was performed using 200–400 ng of RNA with NanoString nCounter technology using the nCounter Human Immunology V2 gene panel (NanoString Technologies) (Supporting Information S1: Table S1). Samples with high expression of nCounter negative control genes were removed from further analysis. Raw count matrices were normalized using RUVg[27] with the housekeeping genes included on the nCounter Human Immunology V2 gene panel. For unsupervised clustering, nonnegative matrix factorization (NMF) was used to determine the number of clusters within the data and to deconvolute the normalized count matrices into matrices describing the metagenes and cluster membership for each sample.[28] Differential gene expression analysis was performed on the raw count matrix using DESeq 2,[29] with the normalization factor from RUVg provided in the design matrix to model technical sample-to-sample variability.[30] An absolute $\log_2$ fold change threshold of 1 and adjusted p value threshold ≤0.2 was used to identify differentially expressed genes.

Hematoxylin and eosin (H&E) staining

FFPE sections were deparaffinized in xylene and hydrated with graded ethanols (100% EtOH, 95% EtOH, 80% EtOH, 2× H_2O). Modified Harris hematoxylin (Epredia™ Modified Harris Hematoxylin) was used in a regressive technique, differentiated in acid alcohol (Epredia™ Richard-Allan Scientific™ Differentiating Solution) and blue color revealed (Epredia™ Signature Series™ Bluing Reagent). Sections were then stained with Eosin (Epredia™ Richard-Allan Scientific™ Eosin-Y Alcoholic, Eosin-Y with Phloxine) followed by routine dehydration. Sections were coverslipped with a permanent, xylene-based mounting media.

Multiplex immunohistochemistry

FFPE tissue slides were stained on a Leica BOND Rx autostainer using the Akoya Opal mIHC assay (Akoya Biosciences), according to the manufacturer's recommendations, with minor modifications. Additional washes were performed after the secondary antibody and Opal fluor applications using high-salt TBST (0.05 M Tris, 0.3 M NaCl, and 0.1% Tween-20, pH 7.2–7.6) and the blocking buffer was TCT (0.05 M Tris, 0.15 M NaCl, 0.25% Casein, 0.1% Tween 20, pH 7.6 ± 0.1). Sections were stained using two mIHC panels. The first panel included antibodies to CD8, CD4, Foxp3, CD14, CD19, and CD56, and the second panel included antibodies to CD3, CD19, CD68/CD163, PD-1, PD-L1, and Ki-67 (Supporting Information S1: Table S2). The CD68/CD163 cocktail stained all cells positive for CD68 and/or CD163. Primary antibodies were incubated for 1 h at room temperature. Tissues were counterstained with 4′,6-diamidino-2-phenylindole (DAPI) to identify nuclei. Slides were mounted with ProLong Gold and cured for 24 h at room temperature in the dark before image acquisition at ×20 magnification on the Akoya Vectra 3.0 Automated or PhenoImager HT Automated Imaging System. Images were spectrally unmixed using Akoya inForm software and exported as multi-image TIFFs for use in the HALO Link image management system (Indica Labs).

Digital image analyses

Images were analyzed with HALO image analysis software (HiPlex FL v3.0.3; Indica Labs). After the cells were visualized based on nuclear and cytoplasmic stains, the mean pixel fluorescence intensity in

applicable compartments of each cell was determined. Positive staining was established by manual adjustment of the mean intensity threshold above the background for each fluorochrome. Positive cell data was then used to define colocalized populations and to perform spatial analyses using nearest neighbor and proximity software (Spatial analysis module). For nearest neighbor analysis, the average distance from each PD-1$^+$ T cell to the nearest PD-L1$^+$ macrophage and PD-L1$^+$ tumor cell was calculated. For proximity analysis, the distance was measured between PD-1$^+$ T cells and PD-L1$^+$ macrophages or tumor cells. Cells were grouped into 20 bins of 5 µm ranging from 0 to >100 µm distance between PD-1$^+$ T cells and PD-L1$^+$ macrophages or tumor cells. The 30 µm threshold was used to calculate the percentage of PD-1$^+$ T cells adjacent to PD-L1$^+$ cells. The CD56 antibody marker was not included in the analysis due to suboptimal staining. Tissue classifier software (Random Forest algorithm trained-by-example, resolution 3.21 µm/pixel, maximum object size 200–810 µm^2) was used with artificial intelligence (AI), machine learning assist to identify and quantitate regions defined by lineage markers CD19 (B/tumor cells), CD3 (T cells), and CD68/CD163 (macrophages). Interspersed regions were defined by adjacent CD19$^+$ tumor cells with single interspersed T cells or macrophages. T-cell and macrophage aggregates were defined as three or more adjacent homotypic cells (i.e., CD3$^+$ or CD68/CD163$^+$, respectively). Hypocellular regions were defined as devoid of all markers and reduced DAPI staining. AI annotation masks were compared with original staining on images for concordance with antibody marker expression and reviewed by a hematopathologist.

Statistical analyses

Median/range and count/percentage were calculated for continuous and categorical variables, respectively. Fisher's exact test was used for comparisons of categorical variables and two-tailed Mann–Whitney test was used for comparisons of continuous variables. A $p < 0.05$ was considered statistically significant. Logistic regression was used for modeling response according to CAR-T cell kinetics and according to CAR-T cell kinetics and pre-LD lactate dehydrogenase (LDH) in patients treated with CD19 CAR T cells. The Kaplan–Meier (KM) method was used to estimate progression-free survival (PFS). The reverse KM method was used to estimate the median follow-up time.[31] Patients not experiencing an event were censored at the date of the last follow-up. Statistical analyses and graphing were performed using RStudio (version 2023.06.1+524, RStudion) and Prism software (version 10.2.3; GraphPad Software).

RESULTS

Imperfect correlation between peak CAR-T cell counts in blood and probability of complete response (CR)

We and others have reported that a higher peak of CAR-T cell counts in blood after infusion is associated with response in patients with R/R LBCL.[2,4,5,32] Using logistic regression, we observed that the estimated probability of achieving CR after CAR-T cell therapy was associated with higher peaks of CD8$^+$ and CD4$^+$ CAR-T cells in blood in patients with R/R LBCL. However, these correlations were imperfect. We identified patients with high peak CAR-T cell counts who did not achieve CR, and conversely, others with lower peak CAR-T cell counts who did achieve CR (Figure 1A,B). Using a multivariable logistic regression model including peak CD8$^+$ or CD4$^+$ CAR-T cell count and pre-LD serum LDH concentration, higher peak CAR-T cell counts were predominantly associated with efficacy in patients with lower LDH levels (Figure 1C,D), with less apparent associations in patients with high pre-LD LDH concentrations. These data demonstrate that factors beyond in vivo CAR-T cell counts impact response in LBCL. Together with the observed associations of inferior CAR-T cell therapy efficacy in LBCL patients with higher pre-LD tumor burden,[1,33–35] these findings suggest that the TME might be one of the key contributors in failure of CAR-T cell immunotherapy in LBCL.

Pretreatment tumor biopsies: Patient/treatment characteristics and outcomes

To investigate the role of the TME, we studied pretreatment tumor biopsies collected from 24 patients who received defined composition autologous CD19 CAR-T cell therapy for LBCL in three investigator-initiated clinical trials (NCT01865617, NCT02706405, NCT03103971; www.clinicaltrials.gov). Twelve patients were treated on a previously reported phase 1/2 clinical trial (NCT01865617) with JCAR014 alone,[1,11,25] eight were treated on a previously reported phase 1b clinical trial (NCT02706405) with JCAR014 in combination with the anti-PD-L1 monoclonal antibody, durvalumab,[36] and four with a CAR-T cell product harboring a fully human CD19-targeted single-chain variable fragment (JCAR021, NCT03103971) (Table 1). The median age of study participants was 61 years (range, 27–76). Fourteen (58%) patients had diffuse LBCL, not otherwise specified (DLBCL, NOS), six (25%) had DLBCL transformed from indolent histology (tDLBCL), and four (17%) had high-grade B-cell lymphoma with *MYC* and *BCL2* and/or *BCL6* rearrangements (double- or triple-hit lymphoma, HGBCL). Twelve (50%) patients had germinal center B-cell (GCB) phenotype and nine (38%) had non-GCB phenotype, based on the Hans algorithm.[37] The biopsy samples were all obtained before LD, a median of 30 days (range, 0–165) before the start of LD. All were reviewed by a hematopathologist and contained viable tissue involved by LBCL. Nine (38%) patients received systemic chemotherapy after biopsy sampling. On restaging after CAR-T cell therapy, nine (38%) patients achieved CR as the best response, while 15 (62%) patients did not achieve CR. The median time to achievement of CR was 28 days (range, 27–48). Only two patients who achieved CR progressed within 6 months after CAR-T cell infusion (2.6 and 3.4 months). At a median follow-up of 29.3 months (95% confidence interval [CI], 23.2–not reached), the median PFS for the whole cohort was 2.6 months (95% CI, 1.4–20.0). The baseline characteristics of patients who did or did not achieve CR after CAR-T cell therapy were similar, except for higher serum LDH concentrations observed before LD in patients who did not achieve CR (Table 1).

Higher macrophage and T-cell dysfunction genes in pretreatment biopsies of patients who did not achieve CR

We used multiplexed gene expression analysis with the NanoString nCounter Immunology V2 panel to study the LBCL TME of patients undergoing CAR-T cell therapy. Ten samples were removed due to high expression of nCounter negative control genes. NMF was used to identify clusters in an unsupervised manner (see section Methods). Four clusters were identified (Figure 2). Cluster 1 represented a single liver biopsy with high expression of genes associated with the complement pathway and infection (*C3*, *C5*, *C6*, *C8A*, *C8B*, *C9*, *MBL2*). Cluster 2 comprised all patients who achieved CR ($n = 6$) and one non-CR patient and was marked by high expression of genes involved in T-cell activation, proliferation, trafficking, and cytokine production

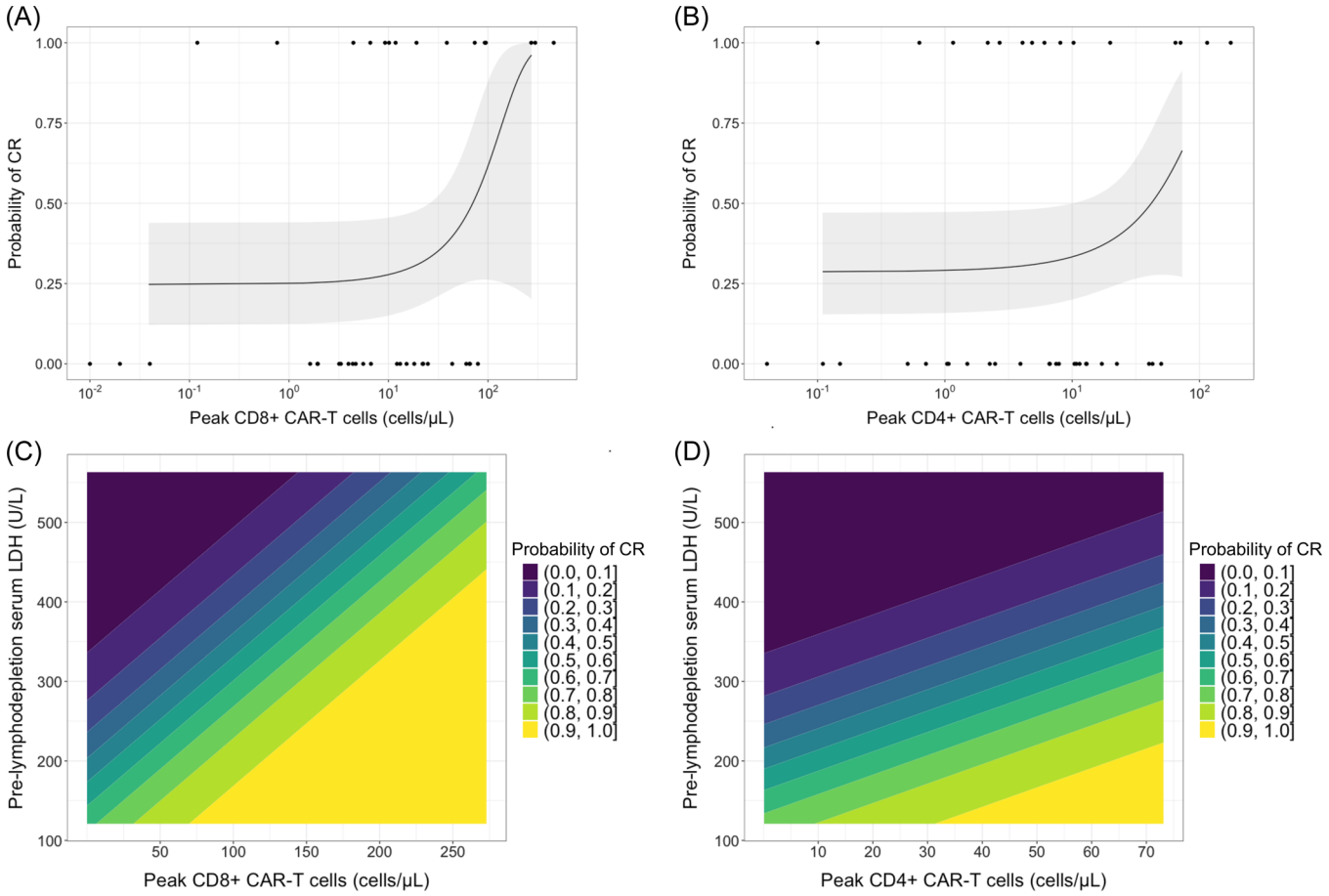

FIGURE 1 Imperfect correlation between peak CAR-T cell counts in blood and probability of response. Peripheral blood samples from patients with R/R LBCL treated with cyclophosphamide and fludarabine lymphodepletion followed by infusion of 2×10^6 CAR-T cells/kg on NCT01865617 were assessed for CAR-T cell enumeration by flow cytometry ($n = 40$). Peak indicates the highest value identified in each patient. (A, B) Estimated probabilities of complete response (CR) by logistic regression according to peak CD8$^+$ (A) and CD4$^+$ (B) CAR-T cell counts in blood. (C, D) Contour plots of estimated probabilities of CR by multivariable logistic regression according to prelymphodepletion lactate dehydrogenase (LDH) and peak CD8$^+$ (C) and CD4$^+$ (D) CAR-T cell counts in blood.

(*IL7R*, *CD44*, *CXCL13*, *CD96*, *CCL19*, *S1PR1*, *EBI3*, *ITGA4*, *TNFRSF9*). Clusters 3 and 4 comprised patients who did not achieve CR; cluster 3 was marked by expression of genes associated with monocytes/macrophages (*CCL2*, *FCGR1A/B*, *CD209*, *ICAM5*, *IL12B*, *IRAK2*, *IDO1*), while cluster 4 was marked by high expression of genes associated with T-cell dysfunction (*CD276*, *LAG3*, *TIGIT*, *CTLA4*) and antigen processing and presentation (*CD74*, HLA genes). These data suggest different transcriptional profiles in the pretreatment LBCL TME are associated with responses to therapy, and that macrophages and T-cell dysfunction might contribute to failure of CAR-T cell therapy for LBCL.

Higher CD4$^+$ T-cell infiltration in pretreatment biopsies of patients who achieved CR

GEP of pretreatment biopsies suggested differences in intratumoral T cells and macrophages might underlie differences in outcomes of patients undergoing CAR-T cell therapy. We therefore performed mIHC analyses to objectively enumerate T cells and macrophages in the TME. Fifteen biopsies with available samples were studied to determine whether the densities of immune cell subsets in the pretreatment TME were associated with the achievement of CR after CAR-T cell therapy. We did not observe significant differences in the densities of total CD3$^+$ T cells between patients who did or did not achieve CR (Figure 3A). However, we noted a higher density of CD4$^+$CD14$^-$ cells in patients who went on to achieve CR (Figure 3B). The absence of CD14 expression was used to exclude monocytic cells that also often express the CD4 molecule.[38] CD4$^+$CD14$^-$ cells were predominantly Foxp3$^-$ and cells with this phenotype were also correlated with achievement of CR (Supporting Information S1: Figure S1A). Foxp3$^+$ cells comprised a small fraction of CD4$^+$CD14$^-$ cells in the TME and were not associated with response (Supporting Information S1: Figure S1B). There were no significant differences in the densities of CD8$^+$ cells, CD68/CD163$^+$ macrophages, CD14$^+$ monocytes, or CD19$^+$ tumor cells between patients who did or did not achieve CR (Figure 3C–E and data not shown).

Morphologic patterns of immune infiltration in the TME correlate with response after CAR-T cell therapy

To investigate differences in immune infiltrates in the pretreatment TME of patients who subsequently did or did not achieve CR after CAR-T cell therapy, we studied the distribution and organization of T cells, macrophages, and tumor cells within the TME. H&E slides,

TABLE 1 Patient and treatment characteristics.

Characteristic	CR (*n* = 9)	Non-CR (*n* = 15)	*p* Value
CD19 CAR-T cell product, number (*n*; %)			
JCAR014	4 (44)	8 (53)	
JCAR014 + durvalumab	2 (22)	6 (40)	
JCAR021	3 (33)	1 (7)	
Age			
Median (interquartile range), years	65 (57–68)	59 (47–66)	0.21
≥65 years, *n* (%)	5 (56)	6 (40)	0.68
Male sex, number (%)	7 (78)	10 (67)	0.67
Disease histology, *n* (%)			
Diffuse large B-cell lymphoma, NOS	6 (67)	8 (53)	0.68
DLBCL transformed from indolent histology	2 (22)	4 (27)	1
High-grade B-cell lymphoma with *MYC* and *BCL2* and/or *BCL6* rearrangements	1 (11)	3 (20)	1
Cell of origin (Hans algorithm), *n* (%)			
Germinal-center B-cell phenotype	6 (67)	6 (40)	0.40
Non-germinal center B-cell phenotype	2 (22)	7 (47)	0.39
Missing	1 (11)	2 (13)	1
MYC rearrangement[a]			
Yes	1 (11)	4 (27)	0.61
No	7 (78)	9 (60)	0.66
Missing	1 (11)	2 (13)	1
Ann Arbor stage III or IV, *n* (%)	9 (100)	13 (87)	0.51
International Prognostic Index (IPI) score, *n* (%)[b]			
0–2	5 (56)	4 (27)	0.22
≥3	4 (44)	11 (73)	0.22
Lactate dehydrogenase (LDH)			
Elevated, *n* (%)	4 (44)	11 (73)	0.22
Median (interquartile range), U/L	164 (132–264)	327 (173–414)	0.03
Tumor cross-sectional area–median (interquartile range), mm^2[c]	3055 (2021–6011)	4829 (2616–10,073)	0.26
Number of prior therapies–median (range)	3 (2–7)	4 (3–8)	0.38
Biopsy day in relation to CAR-T cell infusion–median (range)	−20 (−146 to −6)	−43 (−171 to −5)	0.68
Systemic chemotherapy after biopsy sample, *n* (%)[d]	2 (22)	7 (47)	0.39
Lymphodepletion regimen, *n* (%)			
Cy 60 mg/kg × 1 + Flu 25 mg/m^2 × 3	2 (22)	4 (27)	1
Cy 30 mg/kg × 1 + Flu 25 mg/m^2 × 3	0 (0)	2 (13)	0.51
Cy 300 mg/m^2 × 3 + Flu 30 mg/m^2 × 3	7 (78)	9 (60)	0.66
CAR-T cell dose, *n* (%)			
7×10^5 cell/kg	0	2 (13)	0.51
2×10^6 cell/kg	7 (78)	13 (87)	0.61
7×10^6 cell/kg	2 (22)	0 (0)	0.13

Note: *p* values per Wilcoxon rank-sum test or Fisher's exact test (two-sided), as appropriate.

Abbreviations: Cy, cyclophosphamide; Flu, fludarabine.

[a]*MYC* gene rearrangement by FISH including patients with "double-hit" lymphoma.

[b]Scores on the IPI include low risk (0 or 1 point), low-intermediate risk (2 points), high-intermediate risk (3 points), and high risk (4 or 5 points).

[c]Sum of the product of the perpendicular diameters of up to 6 target measurable nodes and extranodal sites.

[d]Excluding corticosteroids.

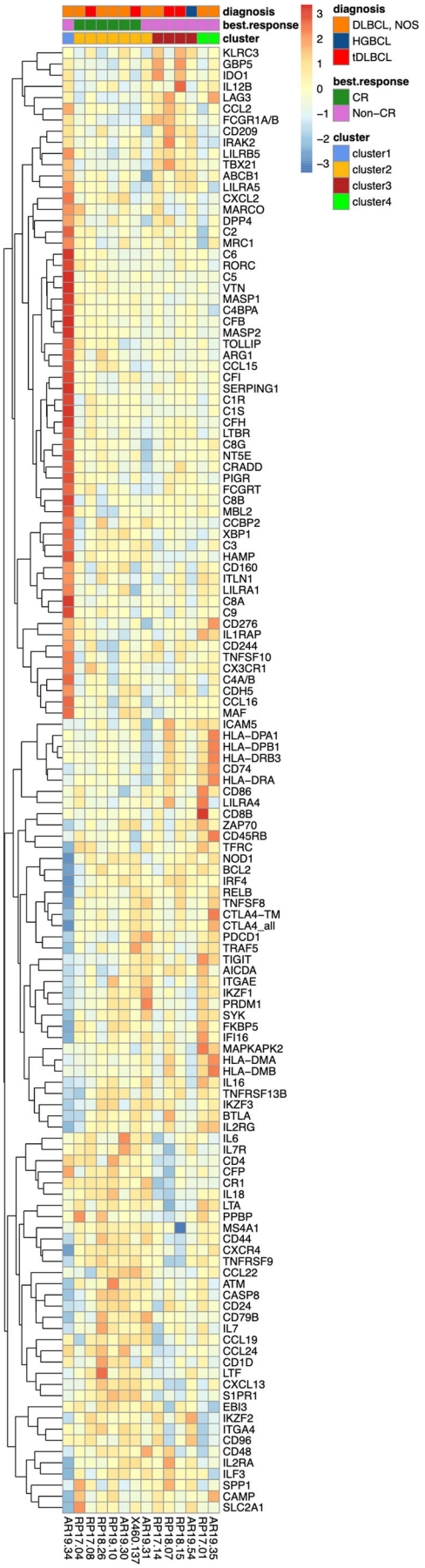

FIGURE 2 Differential gene expression in the pretreatment LBCL TME associated with response after CAR-T cell therapy. Heatmap of gene expression measured by the Immunology V2 panel (NanoString) in pretreatment tumor biopsy specimens ($n = 14$). Nonnegative matrix factorization (NMF) was used to identify clusters in an unsupervised manner. Genes with significant differential expression ($\log_2$ fold change ≥ or <1.0 and adjusted $p \leq 0.2$) between clusters are shown. The color range depicts $\log_2$ normalized expression.

along with mIHC images, were examined by two hematopathologists blinded to the clinical outcomes. Distinct patterns of immune cell infiltration were noted in the TME: T cells and/or macrophages that were interspersed among tumor cells (diffuse); and T cells and/or macrophages that formed aggregates (small/clustered; large/zonal) (Supporting Information S1: Table S3 and Supporting Information S1: Figure S2). Aggregates of T cells and/or macrophages were observed in biopsies from six of seven (86%) patients who achieved CR compared to four of eight (50%) who did not achieve CR ($p = 0.28$) and these aggregates were surrounded by tumor cells and/or in association with fibrotic/sclerotic regions. Five of seven patients with biopsies that harbored fibrosis (71%), compared with only two of eight patients with biopsies without fibrosis (25%), achieved CR ($p = 0.13$). Fibrotic/sclerotic regions were more common in biopsies from patients with tDLBCL compared with patients with DLBCL, NOS (four of five [80%] compared with two of nine [22%], respectively; $p = 0.09$; Supporting Information S1: Table S3).

To further characterize associations between pathologist-identified morphologic patterns and response, we used AI-assisted image analyses to objectively and quantitatively assess the fractions of the biopsies occupied by distinct morphologic patterns and determine their associations with response after CAR-T cell therapy. CD19, CD3, and CD68/CD163 lineage markers (Figure 4A, top) were used for tissue classification, and classifier mask overlays indicated regions classified according to morphologic patterns (Figure 4A, bottom). The regions classified were: (1) interspersed immune infiltrate (red mask), (2) T-cell aggregates (green mask), (3) macrophage aggregates (yellow mask), and (4) hypocellular/fibrotic (blue mask). Interspersed immune infiltrate regions were defined by the predominance of $CD19^+$ tumor cells without clusters of more than three T cells and/or macrophages, corresponding to the diffuse pattern observed in the pathologists' review. T-cell and macrophage aggregates were defined by clusters (more than three) of $CD3^+$ T cells or $CD68/CD163^+$ macrophages, respectively. Hypocellular/fibrotic regions were defined as being devoid of lineage markers, corresponding to fibrosis on the H&E slides (Supporting Information S1: Figure S2D). Biopsies of patients who achieved CR after CAR-T cell therapy harbored a lower proportion occupied by an interspersed immune infiltrate (Figure 4B). There was a trend toward a higher fraction of the biopsy area occupied by T-cell aggregates in patients who achieved CR after CAR-T cell therapy (Figure 4C); whereas there were no significant differences in the fractions of the biopsy area occupied by macrophage aggregates between patients who did or did not achieve CR after CAR-T cell therapy (Figure 4D). Consistent with the finding that fibrosis observed by pathologists on H&E sections associated with response and transformed histology, we observed a higher proportion of AI-classified hypocellular/fibrotic regions in the TME of patients who achieved CR after CAR-T cell therapy (Figure 4E) and a trend toward a higher proportion of AI-classified hypocellular/fibrotic regions in biopsies from patients with tDLBCL (Supporting Information S1: Figure S3D). There was a trend toward a higher fraction of the biopsy area occupied by macrophage aggregates in patients with tDLBCL compared with DLBCL, NOS

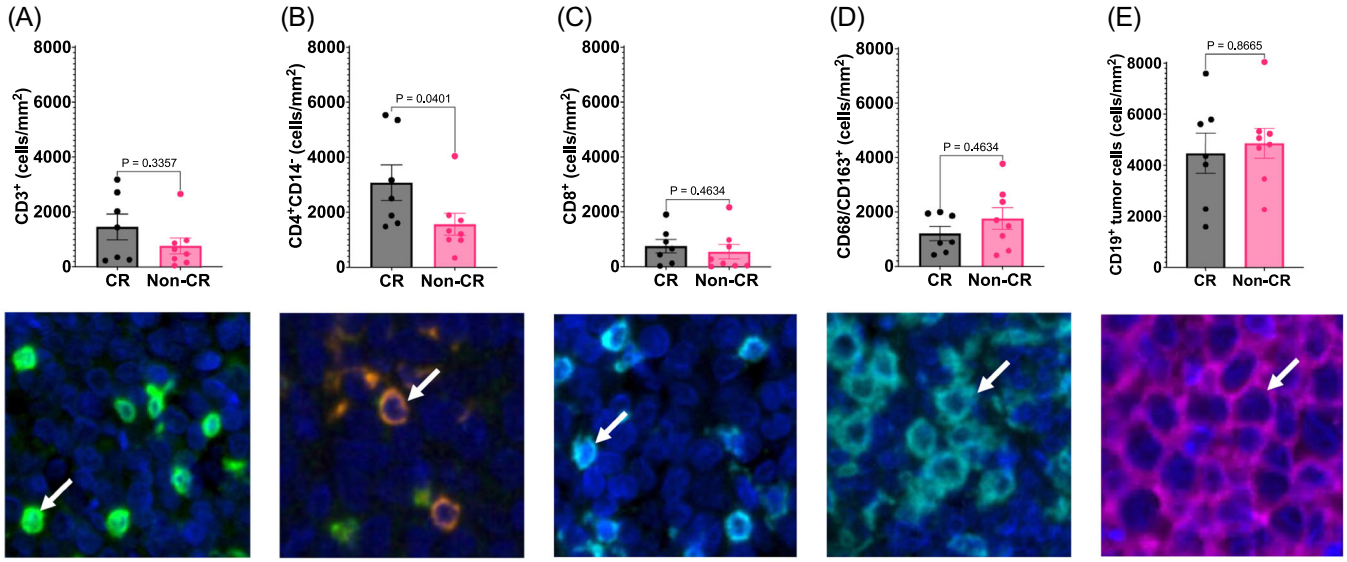

FIGURE 3 Cell densities in pretreatment tumor biopsies. HALO quantification of cell densities of $CD3^+$ cells (A), $CD4^+CD14^-$ cells (B), $CD8^+$ cells (C), $CD68/CD163^+$ macrophages (D), and $CD19^+$ tumor cells (E) in biopsies of patients who did or did not achieve complete response ($n = 15$). Mean ± standard error of the mean (SEM). Two-sided Mann–Whitney tests were used for comparisons between groups. Representative images (×28) of cell types quantified are shown below each graph: CD3 (light green), CD4 (orange), CD14 (dark green), CD8 (cyan), CD68/CD163 cocktail (aqua), and CD19 (magenta). White arrows indicate examples of marker-positive cells.

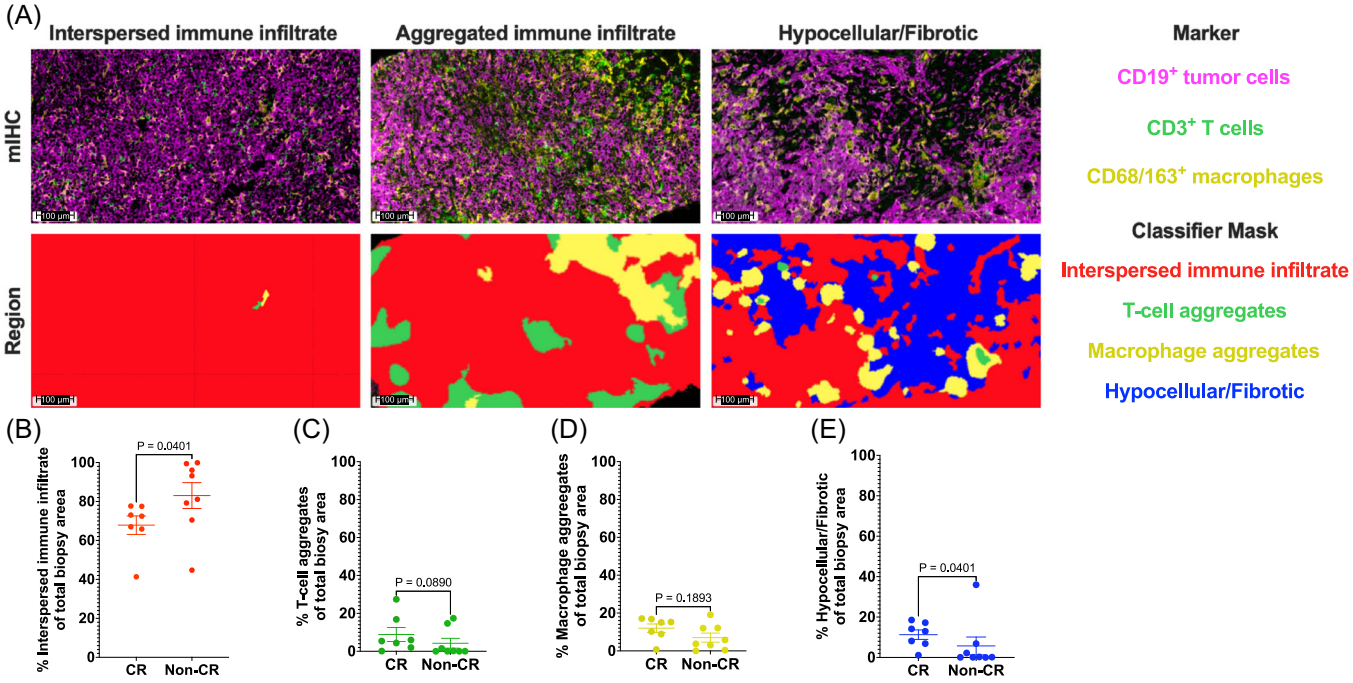

FIGURE 4 AI-assisted image analyses of the tumor microenvironment (TME) architectures in pretreatment biopsies of patients undergoing CAR-T cell therapy. (A) Representative images of the different TME patterns: interspersed immune infiltrate (left), T-cell and macrophage aggregated immune infiltrates (middle), and fibrotic/hypocellular (right). The top row shows representative mIHC images stained with antibodies used for classification, with tumor cells in magenta ($CD19^+$), T cells in green ($CD3^+$), and macrophages in yellow ($CD68/CD163^+$). The bottom row shows classifier masks overlaid onto mIHC images, demonstrating an interspersed immune infiltrate (red), T-cell aggregates (green), macrophage aggregates (yellow), and hypocellular/fibrotic regions (blue). (B–E) Quantification of the areas of interspersed immune infiltrates (B), T-cell aggregates (C), macrophage aggregates (D), and hypocellular/fibrotic regions (E) as a fraction of the total biopsy area in patients who did or did not achieve complete response ($n = 15$). Mean ± standard error of the mean (SEM). Two-sided Mann–Whitney tests were used for comparisons between groups.

(Supporting Information S1: Figure S3C); whereas there were no significant differences in the fractions of the biopsy area occupied by an interspersed immune infiltrate (Supporting Information S1: Figure S3A) and T-cell aggregates (Supporting Information S1: Figure S3B) between the different LBCL histology subtypes. These data suggested that T cells in a TME with predominantly interspersed infiltrate may be more vulnerable and potentially exposed to suppressive signals from adjacent tumor cells.

Higher PD-L1$^+$ macrophages and PD-L1$^+$ tumor cells in pretreatment biopsies from patients who did not achieve CR

Intrinsic T-cell dysfunction due to T-cell exhaustion has been hypothesized as a cause of failure of CAR-T cell immunotherapies.[39] Therefore, we considered that the association between interspersed immune cell infiltration and failure of CAR-T cell therapy might be due to the close proximity between individual infiltrating T cells that express an inhibitory receptor and other cells in the TME that express a cognate inhibitory ligand. Therefore, we examined the expression of PD-1 in T cells and its ligand, PD-L1, in macrophages and tumor cells (Supporting Information S1: Figure S4). While we did not observe a significant difference in the densities of total CD3$^+$ T cells (Figure 3A), we observed a trend toward a higher proportion of CD3$^+$ T cells expressing PD-1 in biopsies from patients who did not achieve CR after CAR-T cell therapy (Figure 5A), consistent with a higher fraction of activated and/or exhausted T cells in these patients. However, the densities of CD3$^+$ T cells expressing PD-1 did not differ between CR and non-CR patients (Figure 5D). Although the densities and fractions of CD68/CD163$^+$ macrophages and CD19$^+$ tumor cells in pretreatment biopsies did not differ between patients who did or did not achieve CR (Figure 3D,E and Supporting Information S1: Figure S5), we observed a trend toward higher proportions of CD68/CD163$^+$ macrophages and significantly higher proportions of CD19$^+$ tumor cells that expressed PD-L1 (Figure 5B,C), as well as correspondingly numerically higher densities of CD68/CD163$^+$PD-L1$^+$ macrophages and significantly higher densities of CD19$^+$PD-L1$^+$ tumor cells (Figure 5E,F) in patients who did not achieve CR. In contrast, the densities and cell proportions of PD-L1$^-$ macrophages and tumor cells were not associated with response (Supporting Information S1: Figure S6). We did not observe differences in CD68/CD163$^+$ macrophages and CD19$^+$ tumor cells expressing PD-L1 according to the LBCL histology subtype (data not shown). A subset of patients was treated with JCAR014 CAR-T cells in combination with the anti-PD-L1 monoclonal antibody, durvalumab. Despite the limited sample size, similar results were observed when the analysis was restricted to patients treated with JCAR014 CAR-T cells alone (Supporting Information S1: Figure S7).

PD-L1 expression was reported to induce macrophage proliferation and polarization toward the anti-inflammatory M2 macrophage phenotype.[40,41] Although our CD68/CD163 macrophage marker cocktail cannot distinguish different macrophage subtypes,

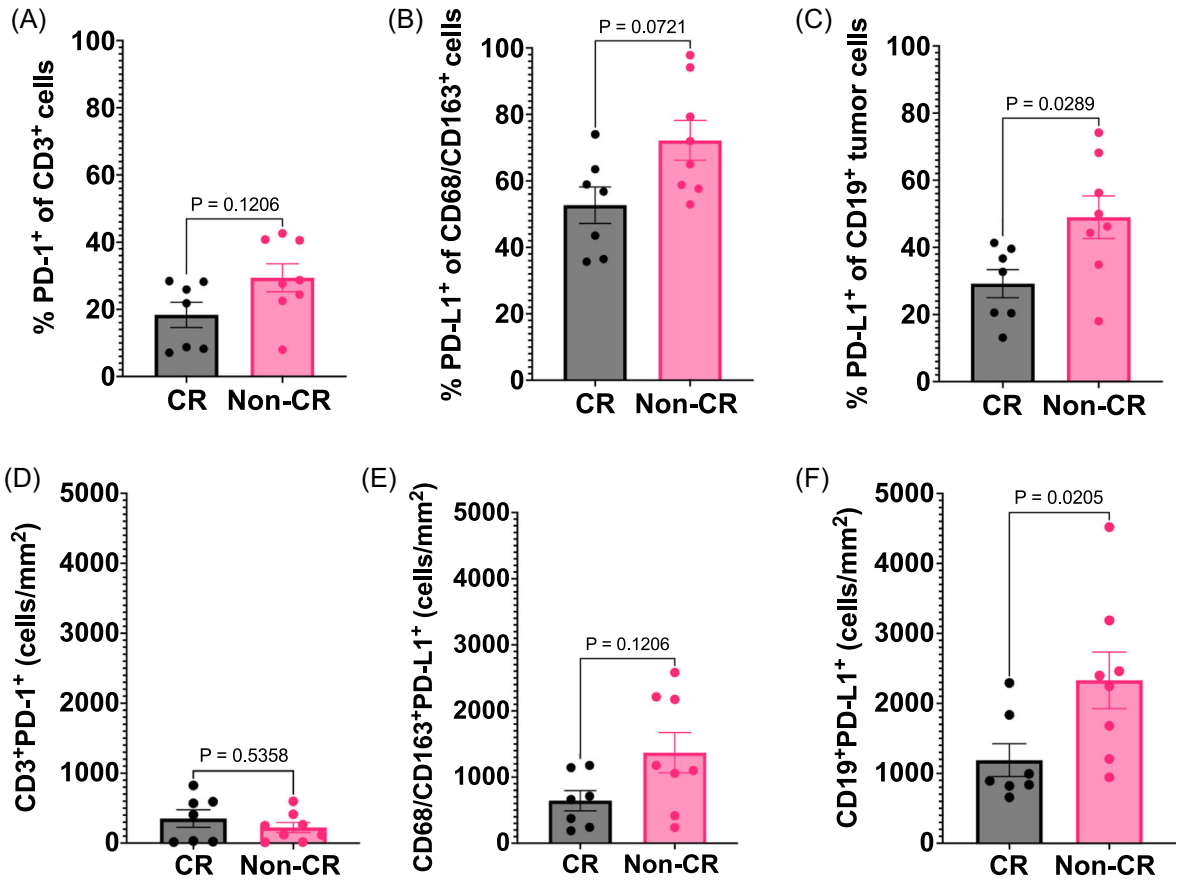

FIGURE 5 PD-1$^+$ T cells and PD-L1$^+$ macrophages and tumor cells in the tumor microenvironment. Proportion of CD3$^+$ T cells that are PD-1 positive (A) and proportion of CD68/CD163$^+$ macrophages (B) and CD19$^+$ tumor cells (C) that are PD-L1 positive in biopsies of patients who did or did not achieve complete response (CR) (n = 15). HALO quantification of cell densities of CD3$^+$PD-1$^+$ T cells (D), CD68/CD163$^+$PD-L1$^+$ (E), and CD19$^+$PD-L1$^+$ tumor cells (F) in biopsies of patients who did or did not achieve CR (n = 15). Mean ± standard error of the mean (SEM). Two-sided Mann–Whitney tests were used for comparisons between groups.

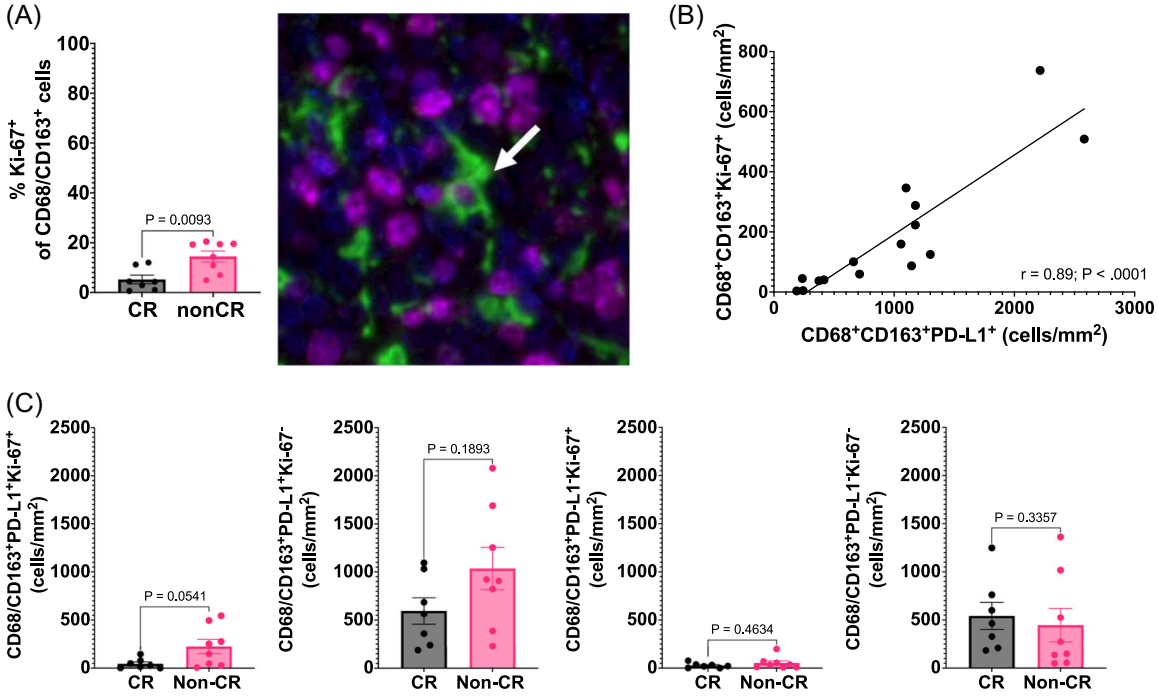

FIGURE 6 Proliferating macrophages are higher in pretreatment biopsies of patients who did not achieve complete response (CR) after CAR-T cell therapy and co-express PD-L1. (A) Proportion of CD68/CD163$^+$ macrophages that co-express Ki-67$^+$ in patients who did or did not achieve CR ($n = 15$). Representative image (×28) of proliferating macrophage is indicated by the white arrow: Ki-67 (magenta), CD68/CD163 (green), 4′,6-diamidino-2-phenylindole (blue). (B) Spearman correlation between CD68/CD163$^+$PD-L1$^+$ and CD68/CD163$^+$Ki-67$^+$ cell densities in pretreatment tumor biopsies. (C) HALO quantification of cell densities of PD-L1$^+$Ki-67$^+$, PD-L1$^+$Ki-67$^-$, PD-L1$^-$Ki-67$^+$, and PD-L1$^-$Ki-67$^-$ phenotype CD68/CD163$^+$ macrophages in pretreatment biopsies of patients who did or did not achieve CR ($n = 15$). Mean ± standard error of the mean (SEM). Two-sided Mann–Whitney tests were used for comparisons between groups.

we noted a higher proportion of Ki-67$^+$ proliferating macrophages in pretreatment biopsies of patients who did not achieve CR after CAR-T cell therapy (Figure 6A) and observed that the cell densities of proliferating Ki-67$^+$ macrophages correlated with the cell densities of PD-L1$^+$ macrophages (Figure 6B). When examining the associations between macrophages expressing PD-L1 and/or Ki-67 and response, we found the strongest association with failure to achieve CR in patients with a higher fraction of macrophages co-expressing both PD-L1 and Ki-67 (Figure 6C).

Spatial analyses demonstrate that the proximity of PD-1$^+$ T cells to PD-L1$^+$ macrophages and tumor cells in pretreatment biopsies is associated with failure to achieve CR

The associations of interspersed immune infiltration and densities of PD-L1$^+$ macrophages, PD-L1$^+$ tumor cells, and proportion of PD-1$^+$ CD3$^+$ T cells with failure to achieve CR prompted us to use nearest neighbor and proximity analyses to objectively determine whether the distance of CD3$^+$ T cells expressing PD-1 to macrophages and/or tumor cells expressing PD-L1 in the pretreatment TME associated with outcomes after CAR-T cell therapy. The average distance from PD-1$^+$ T cells to the nearest PD-L1$^+$ macrophage and from PD-1$^+$ T cells to the nearest PD-L1$^+$ tumor cell was significantly lower in patients who did not achieve CR (Figure 7A,B). Furthermore, a significantly higher proportion of PD-1$^+$ T cells were located in close proximity (<30 μm) to PD-L1$^+$ macrophages and PD-L1$^+$ tumor cells in patients who did not achieve CR (Figure 7C,D and Supporting Information S1: Figure S8). Similar results were observed when the analysis was restricted to patients treated with JCAR014 CAR-T cells alone (Supporting Information S1: Figure S9). The average distance between PD-1$^+$ T cells and PD-L1$^+$ macrophages was higher in biopsies with when compared to those without fibrosis (Supporting Information S1: Figure S10A), which may in part contribute to the better outcomes observed in patients with fibrosis. However, no difference was observed in the average distance between PD-1$^+$ T cells and PD-L1$^+$ tumor cells in biopsies with and without fibrosis (Supporting Information S1: Figure S10B), indicating that the presence of fibrosis alone did not explain the better outcomes observed in these patients.

Together, these data suggest that patterns of immune infiltration in LBCL that results in close proximity of T cells to inhibitory signals from PD-L1$^+$ macrophages and tumor cells may confer a higher risk of T-cell dysfunction and failure of subsequent CAR-T cell therapy.

DISCUSSION

The density, composition, organization, and function of the immune cell infiltrate in the TME have prognostic implications for many cancer immunotherapies[42]; and a plethora of noncancerous cells in the TME regulate the infiltration, accumulation, and proliferation of T cells in tumors.[43] We examined the association between CAR-T cell counts in blood and response after CD19 CAR-T cell immunotherapy in LBCL and found that the relationship between CAR-T cell peak counts and response is imperfect, particularly in those with high pretreatment LDH, a biomarker of tumor burden, proliferation, and poor outcomes in LBCL. This indicates that factors beyond inadequate CAR-T cell counts may contribute to failure of CAR-T cell therapy. While intrinsic

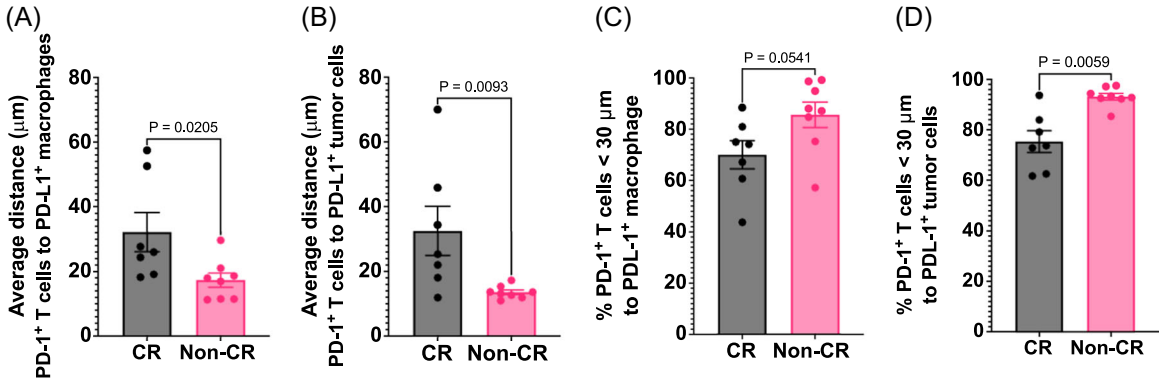

FIGURE 7 Close proximity of PD-1$^+$ T cells to PD-L1$^+$ macrophages and tumor cells in pretreatment biopsies of patients who did not achieve complete response (CR) after CAR-T cell therapy. HALO nearest neighbor analysis was used to calculate the average distance from PD-1$^+$ T cells to the nearest PD-L1$^+$ macrophages (A) and PD-L1$^+$ tumor cells (B) [$n = 15$]. HALO proximity analysis was used to determine the percentage of PD-1$^+$ T cells within 30 μm of PD-L1$^+$ macrophages (C) and PD-L1$^+$ tumor cells (D) [$n = 15$]. Mean ± standard error of the mean (SEM). Two-sided Mann–Whitney tests were used for comparisons between groups.

dysfunction of infused CAR-T cells could contribute, a likely key factor is dysfunction occurring within the LBCL TME. We therefore performed GEP, mIHC, pathology characterization, and spatial analyses to investigate factors in the pretreatment LBCL TME that might be associated with inferior responses to CD19 CAR-T cell immunotherapy.

Transcriptomic profiling of pretreatment biopsies indicated that samples from patients who subsequently achieved CR after CAR-T cell therapy were enriched for genes involved in T-cell activation and infiltration/retention. Corroborating these findings, we showed a higher density of CD4$^+$ T cells by mIHC in pretreatment biopsies of patients who subsequently achieved CR. Our studies were conducted in patients who received CD19 CAR-T cells incorporating a 4-1BB-costimulated CAR. Of note, our findings are supported by those in patients treated with axicabtagene ciloleucel, in which pretreatment biopsies enriched for leukocyte cell–cell adhesion and lymphocyte co-stimulation pathways were also associated with CR.[22] Our GEP data also showed that the TME expression of macrophage and T-cell dysfunction genes was associated with failure to achieve CR after CAR-T cell therapy.

The characterization of the immune landscape in the TME has led to the notion that tumors can be broadly divided into inflamed and noninflamed phenotypes.[44] In our study, distinct morphologic patterns of immune infiltration correlated with the achievement of response. While classification by pathology review suggested an association of favorable response with immune cell aggregates and fibrosis in pretreatment biopsies, AI-assisted classification and quantitation of the areas occupied by distinct immune-infiltrated region patterns provided objective confirmation of the better and worse outcomes associated with fibrosis and interspersed immune infiltration, respectively. The use of AI assistance in analyses of pathology images will be an important factor moving forward to support and validate discoveries made by human morphological assessment.

Our AI-assisted analyses demonstrated that patients who did not achieve CR after CAR-T cell therapy had a higher proportion of their biopsies occupied by an interspersed immune infiltrate, suggesting that T cells could be more vulnerable and exposed to suppressive signals from adjacent cells in the TME. Despite similar densities and fractions of macrophages and tumor cells in patients who did or did not achieve CR, we observed a higher abundance of PD-L1-expressing macrophages and PD-L1-expressing tumor cells in nonresponders. These findings support the conclusion that a more immunosuppressive TME can contribute to T-cell dysfunction, independent of the densities of macrophages and lymphoma cells. A subset of patients included in this study was treated with CAR-T cells combined with the anti-PD-L1 monoclonal antibody, durvalumab. The small numbers precluded the analysis of these associations in this subgroup of patients. Nevertheless, our results are consistent with other studies that showed tumor cells expressing PD-L1[13] and macrophages expressing PD-L1,[23] consistent with an anti-inflammatory M2 phenotype,[40,41] were higher in pretreatment biopsies of patients who had worse outcomes after CAR-T cell therapy. Remarkably, our study further extended these findings by showing the strongest association with failure to respond to CAR-T cells was the density of macrophages co-expressing PD-L1 and Ki-67 in patients who did not achieve CR. These findings could explain some of the inconsistent reports of the associations of PD-L1$^+$ macrophages with outcomes of LBCL.[21,45] Together, our data suggest that proliferating PD-L1$^+$ macrophages might be a key cell type responsible for suppression of CAR-T cell activity in LBCL.

We found that the close proximity of PD-1$^+$ T cells to PD-L1$^+$ macrophages and tumor cells in pretreatment biopsies was associated with failure to achieve CR after CAR-T cell therapy. These results highlight the importance of the spatial relationship of effector and suppressive cells in the TME impacting the response to immunotherapies and demonstrate that the discovery of factors governing the fate of CAR-T cells will be enhanced by investigating the spatial organization of the TME in addition to quantitative and phenotypic studies.

We identified an association between fibrosis and better outcomes of CAR-T cell immunotherapy by pathology review and confirmed by AI-assisted image analyses. Supporting these data, stromal gene signatures were associated with survival in patients with LBCL treated in the chemoimmunotherapy era. The stromal-1 signature, reflecting extracellular matrix deposition and histiocytic infiltration, was associated with a favorable prognosis.[14] This gene set was also higher in pretreatment biopsies of patients who achieved CR after lisocabtagene maraleucel (liso-cel) and was the most correlated to posttreatment T-cell infiltration in the TME.[23] In contrast, a high stromal and immunosuppressive index in pretreatment biopsies was associated with worse duration of response after axicabtagene ciloleucel.[46] In addition to stroma and myeloid cells, this signature also includes immunosuppressive and hypoxia genes, which might contribute to the different findings. We also observed an association between fibrosis and transformed B-cell lymphoma histology. Patients with tDLBCL had a trend toward higher overall response rate

and longer duration of response after liso-cel compared with other LBCL subtypes,[4] and an elevated follicular lymphoma-like gene expression signature, regardless of the histology subtype, was the strongest predictor of response after liso-cel.[23] Our findings suggest that fibrosis might play a role in these associations and warrant further investigation. While the presence of fibrosis might shield aggregates of immune cells from suppressive tumor cells or reflect immune cell-stromal interactions in the TME,[47] the mechanisms by which fibrosis confers a better outcome of CAR-T cell immunotherapy remain unknown. An additional hypothesis is that fibrotic lesions in the TME might support stromal production of immune chemoattractant and adhesion molecules to encourage T-cell infiltration and retention in the TME.

Our study has several limitations including the small sample size and heterogeneity in histologic subtypes and CAR-T cell immunotherapy regimen. However, our results identify morphologic patterns and macrophage and tumor subsets with associations with worse outcomes of CD19 CAR-T cell immunotherapy for LBCL, providing opportunities to investigate modification of the TME to improve efficacy of CAR-T cells. The study supports investigation of the spatial topography of the TME as a predictor of response to CD19 CAR-T cell immunotherapy for LBCL.

ACKNOWLEDGMENTS

The authors thank the staff of the Fred Hutchinson Cancer Center (Fred Hutch) Cell Processing Facility, Fred Hutch Cell Therapy Laboratory, Fred Hutch Integrated Immunotherapy Research Center, Fred Hutch Bezos Family Immunotherapy Clinic, and Fred Hutch Experimental Histopathology and Clinical Trials Pathology laboratories.

AUTHOR CONTRIBUTIONS

Alexandre V. Hirayama, Jocelyn H. Wright, and Cameron J. Turtle conceived and designed research studies. Jocelyn H. Wright and Kimberly S. Smythe performed experiments. Cecilia C. S. Yeung managed the processing, histology, storage, and maintenance of the specimens for the studies and performed QA/QC for the mIHC images. Cecilia C. S. Yeung and Kikkeri N. Naresh reviewed pathology cases and mIHC images. Alexandre V. Hirayama and Jocelyn H. Wright collected data. Alexandre V. Hirayama, Jocelyn H. Wright, and Cameron J. Turtle analyzed and interpreted data. Alexandre V. Hirayama, Jocelyn H. Wright, and Akira N. Shaw performed statistical analyses. Alexandre V. Hirayama, Jocelyn H. Wright, and Cameron J. Turtle wrote the manuscript; and all authors reviewed and edited the final version of the manuscript.

CONFLICT OF INTEREST STATEMENT

Alexandre V. Hirayama has received research funding from Juno Therapeutics, a Bristol Myers Squibb Company, and Nektar Therapeutics; has received honoraria from Bristol Myers Squibb. Kimberly S. Smythe has received consulting/honoraria from Sensei Biotherapeutics. Salvatore Fiorenza reports grants from Bristol Myers Squibb and other support in the form of pending equity from Link Immunotherapeutics outside of the submitted work; has issued patents for PCT/US2021/025255 and PCT/US2021/025248d, and a patent for PCT/US2021/025260 issued, licensed, and with royalties paid from Bristol Myers Squibb. Jordan Gauthier has received research funding from Sobi, Juno Therapeutics, a Bristol Myers Squibb Company, Celgene, and Angiocrine Bioscience; has received consulting/honoraria from Sobi, Legend Biotech, Janssen, Kite Pharma, a Gilead company, and MorphoSys. Cecilia C. S. Yeung has received research funding from OBI, Lonza, Sensei, Signal One, and Pfizer; serves on scientific advisory boards for Twinstrand Biosciences, Abbvie, Eli Lily, and Loxo. David G. Maloney has received research funding from Juno Therapeutics, a Bristol Myers Squibb Company, Celgene, and Kite Pharma, a Gilead company; has served on ad hoc advisory board meetings from Amgen, BMS, Genentech, Gilead, Incyte, Janssen, Legend Biotech, Mustang Bio, MorphoSys, Novartis, Pharmacyclics, and Umoja; has rights to receive royalties from Fred Hutch for patents licensed to Juno Therapeutics; serves on scientific advisory board with stock options and compensations for A2 Biotherapeutics and Navan Technologies. Cameron J. Turtle has received research funding from Juno Therapeutics, a Bristol Myers Squibb Company, NanoString Technologies, and Nektar Therapeutics; has served on scientific and consulting roles in the last 12 months for Caribou Biosciences, T-CURX, Myeloid Therapeutics, ArsenalBio, Cargo Therapeutics, Differentia Bio, Advesya, eGlint, Celgene/Bristol Myers Squibb Cell Therapy, Novartis, Prescient Therapeutics, Century Therapeutics, IGM Biosciences, and Abbvie; serves on a DSMB for Kyverna; has stock options in Eureka Therapeutics, Caribou Biosciences, Myeloid Therapeutics, Cargo Therapeutics, and ArsenalBio; and has the right to receive payments from Fred Hutchinson Cancer Center as an inventor on patents related to CAR-T cell therapy. The remaining authors have no conflicts of interest to report related to this work.

DATA AVAILABILITY STATEMENT

De-identified individual participant data may be requested by contacting the corresponding author.

FUNDING

This work was supported by National Institutes of Health (NIH) National Cancer Institute grants R01 CA136551 and P30 CA15704, NIH National Institute of Diabetes and Digestive and Kidney Diseases grant P30 DK56465, NIH National Heart, Lung, and Blood Institute funded National Gene Vector Biorepository at Indiana University (Contract # 75N92019D00018), Life Science Discovery Fund, the Bezos family, Fred Hutch Immunotherapy Integrated Research Center, Lymphoma Research Foundation, Juno Therapeutics, a BMS Company, NanoString Technologies, and the CLEARbridge Foundation. A.V.H. is supported by the Lymphoma Research Foundation (LRF) Post-Doctoral Fellowship Grant. The other authors received no specific funding for this work.

ORCID

Alexandre V. Hirayama https://orcid.org/0000-0001-7980-3882

SUPPORTING INFORMATION

Additional supporting information can be found in the online version of this article.

REFERENCES

1. Hirayama AV, Gauthier J, Hay KA, et al. The response to lymphodepletion impacts PFS in patients with aggressive non-Hodgkin lymphoma treated with CD19 CAR T cells. *Blood*. 2019;133(17):1876-1887. doi:10.1182/blood-2018-11-887067
2. Neelapu SS, Locke FL, Bartlett NL, et al. Axicabtagene ciloleucel CAR T-cell therapy in refractory large B-cell lymphoma. *N Engl J Med*. 2017;377(26):2531-2544. doi:10.1056/NEJMoa1707447
3. Schuster SJ, Bishop MR, Tam CS, et al. Tisagenlecleucel in adult relapsed or refractory diffuse large B-cell lymphoma. *N Engl J Med*. 2019;380(1):45-56. doi:10.1056/NEJMoa1804980
4. Abramson JS, Palomba ML, Gordon LI, et al. Lisocabtagene maraleucel for patients with relapsed or refractory large B-cell

lymphomas (TRANSCEND NHL 001): a multicentre seamless design study. *Lancet*. 2020;396:839-852. doi:10.1016/S0140-6736(20)31366-0
5. Locke FL, Miklos DB, Jacobson CA, et al. Axicabtagene ciloleucel as second-line therapy for large B-cell lymphoma. *N Engl J Med*. 2022;386(7):640-654. doi:10.1056/NEJMoa2116133
6. Bishop MR, Dickinson M, Purtill D, et al. Second-line tisagenlecleucel or standard care in aggressive B-cell lymphoma. *N Engl J Med*. 2022;386(7):629-639. doi:10.1056/NEJMoa2116596
7. Kamdar M, Solomon SR, Arnason J, et al. Lisocabtagene maraleucel versus standard of care with salvage chemotherapy followed by autologous stem cell transplantation as second-line treatment in patients with relapsed or refractory large B-cell lymphoma (TRANSFORM): results from an interim analysis of an open-label, randomised, phase 3 trial. *Lancet (London, England)*. 2022;399(10343):2294-2308. doi:10.1016/S0140-6736(22)00662-6
8. Spiegel JY, Patel S, Muffly L, et al. CAR T cells with dual targeting of CD19 and CD22 in adult patients with recurrent or refractory B cell malignancies: a phase 1 trial. *Nat Med*. 2021;27(8):1419-1431. doi:10.1038/s41591-021-01436-0
9. Deng Q, Han G, Puebla-Osorio N, et al. Characteristics of anti-CD19 CAR T cell infusion products associated with efficacy and toxicity in patients with large B cell lymphomas. *Nat Med*. 2020;26:1878-1887. doi:10.1038/s41591-020-1061-7
10. Jackson Z, Hong C, Schauner R, et al. Sequential single-cell transcriptional and protein marker profiling reveals TIGIT as a marker of CD19 CAR-T cell dysfunction in patients with non-Hodgkin lymphoma. *Cancer Discovery*. 2022;12(8):1886-1903. doi:10.1158/2159-8290.Cd-21-1586
11. Hirayama AV, Gauthier J, Hay KA, et al. High rate of durable complete remission in follicular lymphoma after CD19 CAR-T cell immunotherapy. *Blood*. 2019;134(7):636-640. doi:10.1182/blood.2019000905
12. Yan ZX, Li L, Wang W, et al. Clinical efficacy and tumor microenvironment influence in a dose-escalation study of anti-CD19 chimeric antigen receptor T cells in refractory B-cell non-Hodgkin's lymphoma. *Clin Cancer Res*. 2019;25(23):6995-7003. doi:10.1158/1078-0432.CCR-19-0101
13. Jain MD, Zhao H, Wang X, et al. Tumor interferon signaling and suppressive myeloid cells are associated with CAR T-cell failure in large B-cell lymphoma. *Blood*. 2021;137(19):2621-2633. doi:10.1182/blood.2020007445
14. Lenz G, Wright G, Dave SS, et al. Stromal gene signatures in large-B-cell lymphomas. *N Engl J Med*. 2008;359(22):2313-2323. doi:10.1056/NEJMoa0802885
15. Alizadeh AA, Gentles AJ, Alencar AJ, et al. Prediction of survival in diffuse large B-cell lymphoma based on the expression of 2 genes reflecting tumor and microenvironment. *Blood*. 2011;118(5):1350-1358. doi:10.1182/blood-2011-03-345272
16. Ciavarella S, Vegliante MC, Fabbri M, et al. Dissection of DLBCL microenvironment provides a gene expression-based predictor of survival applicable to formalin-fixed paraffin-embedded tissue. *Ann Oncol*. 2018;29(12):2363-2370. doi:10.1093/annonc/mdy450
17. Kotlov N, Bagaev A, Revuelta MV, et al. Clinical and biological subtypes of B-cell lymphoma revealed by microenvironmental signatures. *Cancer Discovery*. 2021;11(6):1468-1489. doi:10.1158/2159-8290.Cd-20-0839
18. Keane C, Gill D, Vari F, Cross D, Griffiths L, Gandhi M. $CD4^+$ tumor-infiltrating lymphocytes are prognostic and independent of R-IPI in patients with DLBCL receiving R-CHOP chemo-immunotherapy. *Am J Hematol*. 2013;88(4):273-276. doi:10.1002/ajh.23398
19. Lin M, Ma S, Sun L, Qin Z. The prognostic value of tumor-associated macrophages detected by immunostaining in diffuse large B cell lymphoma: a meta-analysis. *Front Oncol*. 2023;12:1094400. doi:10.3389/fonc.2022.1094400
20. Kiyasu J, Miyoshi H, Hirata A, et al. Expression of programmed cell death ligand 1 is associated with poor overall survival in patients with diffuse large B-cell lymphoma. *Blood*. 2015;126(19):2193-2201. doi:10.1182/blood-2015-02-629600
21. Xu-Monette ZY, Xiao M, Au Q, et al. Immune profiling and quantitative analysis decipher the clinical role of immune-checkpoint expression in the tumor immune microenvironment of DLBCL. *Cancer Immunol Res*. 2019;7(4):644-657. doi:10.1158/2326-6066.Cir-18-0439
22. Scholler N, Perbost R, Locke FL, et al. Tumor immune contexture is a determinant of anti-CD19 CAR T cell efficacy in large B cell lymphoma. *Nat Med*. 2022;28(9):1872-1882. doi:10.1038/s41591-022-01916-x
23. Olson NE, Ragan SP, Reiss DJ, et al. Exploration of tumor biopsy gene signatures to understand the role of the tumor microenvironment in outcomes to lisocabtagene maraleucel. *Mol Cancer Ther*. 2023;22(3):406-418. doi:10.1158/1535-7163.MCT-21-0506
24. Turtle CJ, Hanafi LA, Berger C, et al. CD19 CAR-T cells of defined CD4+:CD8+ composition in adult B cell ALL patients. *J Clin Invest*. 2016;126(6):2123-2138. doi:10.1172/jci85309
25. Turtle CJ, Hanafi LA, Berger C, et al. Immunotherapy of non-Hodgkin's lymphoma with a defined ratio of $CD8^+$ and $CD4^+$ CD19-specific chimeric antigen receptor-modified T cells. *Sci Transl Med*. 2016;8(355):355ra116. doi:10.1126/scitranslmed.aaf8621
26. Cheson BD, Fisher RI, Barrington SF, et al. Recommendations for initial evaluation, staging, and response assessment of Hodgkin and non-Hodgkin lymphoma: the Lugano classification. *J Clin Oncol*. 2014;32(27):3059-3067. doi:10.1200/jco.2013.54.8800
27. Risso D, Ngai J, Speed TP, Dudoit S. Normalization of RNA-seq data using factor analysis of control genes or samples. *Nat Biotechnol*. 2014;32(9):896-902. doi:10.1038/nbt.2931
28. Brunet JP, Tamayo P, Golub TR, Mesirov JP. Metagenes and molecular pattern discovery using matrix factorization. *Proc Natl Acad Sci USA*. 2004;101(12):4164-4169. doi:10.1073/pnas.0308531101
29. Love MI, Huber W, Anders S. Moderated estimation of fold change and dispersion for RNA-seq data with DESeq2. *Genome Biol*. 2014;15(12):550. doi:10.1186/s13059-014-0550-8
30. Bhattacharya A, Hamilton AM, Furberg H, et al. An approach for normalization and quality control for NanoString RNA expression data. *Brief. Bioinform*. 2021;22(3):bbaa163. doi:10.1093/bib/bbaa163
31. Schemper M, Smith TL. A note on quantifying follow-up in studies of failure time. *Controlled Clin Trials*. 1996;17(4):343-346.
32. Hay KA, Hanafi LA, Li D, et al. Kinetics and biomarkers of severe cytokine release syndrome after CD19 chimeric antigen receptor-modified T-cell therapy. *Blood*. 2017;130(21):2295-2306. doi:10.1182/blood-2017-06-793141
33. Dean EA, Mhaskar RS, Lu H, et al. High metabolic tumor volume is associated with decreased efficacy of axicabtagene ciloleucel in large B-cell lymphoma. *Blood Adv*. 2020;4(14):3268-3276. doi:10.1182/bloodadvances.2020001900
34. Vercellino L, Di Blasi R, Kanoun S, et al. Predictive factors of early progression after CAR T-cell therapy in relapsed/refractory diffuse large B-cell lymphoma. *Blood Adv*. 2020;4(22):5607-5615. doi:10.1182/bloodadvances.2020003001
35. Iacoboni G, Simó M, Villacampa G, et al. Prognostic impact of total metabolic tumor volume in large B-cell lymphoma patients receiving CAR T-cell therapy. *Ann Hematol*. 2021;100(9):2303-2310. doi:10.1007/s00277-021-04560-6
36. Hirayama AV, Kimble EL, Wright JH, et al. Timing of anti-PD-L1 antibody initiation affects efficacy/toxicity of CD19 CAR T-cell therapy for large B-cell lymphoma. *Blood Adv*. 2024;8(2):453-467. doi:10.1182/bloodadvances.2023011287

37. Hans CP, Weisenburger DD, Greiner TC, et al. Confirmation of the molecular classification of diffuse large B-cell lymphoma by immunohistochemistry using a tissue microarray. *Blood*. 2004;103(1):275-282. doi:10.1182/blood-2003-05-1545
38. Zhen A, Krutzik SR, Levin BR, Kasparian S, Zack JA, Kitchen SG. CD4 ligation on human blood monocytes triggers macrophage differentiation and enhances HIV infection. *J Virol*. 2014;88(17):9934-9946. doi:10.1128/jvi.00616-14
39. Shah NN, Fry TJ. Mechanisms of resistance to CAR T cell therapy. *Nat Rev Clin Oncol*. 2019;16(6):372-385. doi:10.1038/s41571-019-0184-6
40. Lu D, Ni Z, Liu X, et al. Beyond T cells: understanding the role of PD-1/PD-L1 in tumor-associated macrophages. *J Immunol Res*. 2019;2019:1919082. doi:10.1155/2019/1919082
41. Li W, Wu F, Zhao S, Shi P, Wang S, Cui D. Correlation between PD-1/PD-L1 expression and polarization in tumor-associated macrophages: a key player in tumor immunotherapy. *Cytokine Growth Factor Rev*. 2022;67:49-57. doi:10.1016/j.cytogfr.2022.07.004
42. Fridman WH, Zitvogel L, Sautès–Fridman C, Kroemer G. The immune contexture in cancer prognosis and treatment. *Nat Rev Clin Oncol*. 2017;14(12):717-734734. doi:10.1038/nrclinonc.2017.101
43. Joyce JA, Fearon DT. T cell exclusion, immune privilege, and the tumor microenvironment. *Science*. 2015;348(6230):74-80. doi:10.1126/science.aaa6204
44. Chen DS, Mellman I. Elements of cancer immunity and the cancer-immune set point. *Nature*. 2017;541(7637):321-330. doi:10.1038/nature21349
45. McCord R, Bolen CR, Koeppen H, et al. PD-L1 and tumor-associated macrophages in de novo DLBCL. *Blood Adv*. 2019;3(4):531-540. doi:10.1182/bloodadvances.2018020602
46. Locke FL, Filosto S, Chou J, et al. Impact of tumor microenvironment on efficacy of anti-CD19 CAR T cell therapy or chemotherapy and transplant in large B cell lymphoma. *Nat Med*. 2024;30:507-518. doi:10.1038/s41591-023-02754-1
47. Bhattacharya M, Ramachandran P. Immunology of human fibrosis. *Nat Immunol*. 2023;24(9):1423-1433. doi:10.1038/s41590-023-01551-9